Refractive Effects of Planar Protective Layers in Stereo Photogrammetry and Their Correction

Zhaoquan Liu [1], Binbin Xu [2], Wenxing Xu [3], Shigang Liu [4], Yongfeng Ma [5], Guanqing Li [6,*]

[1] CCCC First Harbor Engineering Company Ltd., 300461 Tianjin, China – liuzhaoquan@cccltd.cn
[2] No.3 Engineering Company Ltd. of CCCC First Harbor Engineering Company, 116011 Dalian, China; CCCC First Harbor Engineering Company Ltd., 300461 Tianjin, China; Key Laboratory of Geotechnical Engineering, CCCC, 300461 Tianjin, China; Key Laboratory of Port Geotechnical Engineering, Ministry of Transport, PRC, 300461 Tianjin, China; Key Laboratory of Port Geotechnical Engineering of Tianjin, Tianjin 300461, China – 2016046927@cccltd.cn
[3] No.3 Engineering Company Ltd. of CCCC First Harbor Engineering Company, 116011 Dalian, China – xuwenxing1@cccltd.cn
[4] No.3 Engineering Company Ltd. of CCCC First Harbor Engineering Company, 116011 Dalian, China – liushigang1@cccltd.cn
[5] No.3 Engineering Company Ltd. of CCCC First Harbor Engineering Company, 116011 Dalian, China – mayongfeng1@cccltd.cn
[6,*] School of Environment and Spatial Informatics, China University of Mining and Technology, 221116 Xuzhou, China – guanqing.li@cumt.edu.cn

Keywords: Stereo Photogrammetry, Planar Protective Layer, Refractive Effects, Ray Tracing, Correction Method, 3D Monitoring.

Abstract

Vision-based measurement is widely used in structural monitoring. However, in complex environments such as tunnels, dusty areas, or explosion-proof scenarios, cameras are often installed behind protective windows, which introduce refractive effects that degrade measurement accuracy if conventional air-based imaging models are applied. This study investigates the refractive effects induced by a planar protective layer in an air–protective layer–air medium configuration. A binocular vision measurement model considering the planar protective layer is established based on ray tracing and geometric refraction principles. Simulation experiments are conducted to quantitatively analyse the influence of factors such as target-to-camera distance, protective layer pose, thickness, and camera-to-layer distance on reconstruction accuracy. The results show that neglecting the protective layer leads to significant systematic errors, particularly in the depth direction, while the proposed refraction-aware model effectively eliminates these deviations. Field experiments performed under different environmental conditions further confirm that the corrected reconstruction results are closely consistent with the ground truth and that systematic errors are significantly reduced. The study demonstrates that accurate modelling and calibration of refractive parameters are essential for reliable stereo vision measurements in cross-media environments, providing a practical reference for engineering applications involving protective windows.

1. Introduction

Vision-based measurement offers advantages such as high accuracy, multi-point capability, rapid acquisition, and non-contact operation, and has been widely applied in large-scale structural monitoring, defect detection, and slope monitoring (Zhan et al., 2024; Chen rt al., 2020). However, in complex environments such as tunnels with water mist, dust, or explosion-proof requirements, cameras must be specially designed with protective enclosures, and imaging is performed through a protective layer (Yang et al., 2021a).

The protective layer is typically a transparent glass plate. When light passes through this layer, refraction occurs, causing the object point, image point, and camera optical centre to no longer lie on a straight line. If the conventional single-viewpoint imaging model is still adopted for data processing, measurement accuracy will be degraded (Treibitz et al., 2012). Refraction correction in multi-medium environments has attracted extensive attention in the field of underwater vision measurement. On the one hand, refraction effects can be treated as geometric distortions and mitigated by calibrating intrinsic camera parameters such as focal length (Li et al., 2018; Hu et al., 2024). On the other hand, refractive imaging models can be established based on the geometric configuration of refracted rays to explicitly compensate for multi-medium imaging effects (Wu et al., 2023; Su et al., 2021). Such models introduce additional parameters, including the normal vector of the refractive interface and the distance between the interface and the camera, which must be calibrated in advance in practical applications (Li et al., 2024; Tong et al., 2023).

Non-single-medium vision measurement has gradually been extended to environments with fog, dust, and explosion-proof requirements. Compared with underwater scenarios, studies on refraction effects and their correction under air–protective layer–air conditions are relatively limited, with only a few works addressing refractive distortion correction in monocular vision systems (Yang et al., 2021b). Therefore, this paper focuses on a binocular vision measurement scenario with a planar protective layer. First, a binocular vision measurement model considering the planar protective layer is established. Then, simulation experiments are conducted to systematically analyse the influence of factors such as the object-to-camera distance, the distance between the protective layer and the camera, the pose and thickness of the protective layer on measurement results, and comparisons are made with the conventional binocular measurement method that ignores the protective layer. Finally, field experiments are carried out to validate the proposed model and refraction correction method. The main contribution of this study lies in quantitatively evaluating the magnitude and applicable boundaries of refractive effects introduced by a planar protective layer in binocular vision measurement, providing a reference for model selection, parameter calibration, and accuracy assessment of binocular vision systems in complex environments such as explosion-proof and dust-laden conditions.

https://doi.org/10.5194/isprs-archives-XLIX-B2-2026-1043-2026

2. Methodology

2.1 Imaging geometry with a planar protective layer

A planar protective layer is mounted in front of the stereo cameras. The layer is a flat plate made of (organic) glass with a certain thickness. As illustrated in Figure 1, the light propagating from the target to the camera optical centre undergoes two refractions at the surfaces of the protective layer, such that the target point, the image point, and the camera optical centre are no longer collinear. The point P is defined as the intersection of the rays PL_4 and PR_4. To compute its coordinates, the following assumptions are made.

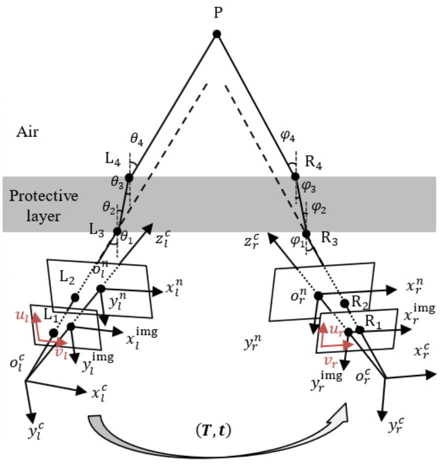

Figure 1. Light path of stereo photogrammetry with planar protective layers

(1) The intrinsic parameters of the left and right cameras, $\boldsymbol{K}_l$ and $\boldsymbol{K}_r$, are known from camera calibration.

(2) Taking the left camera coordinate system $o_l^c - x_l^c y_l^c z_l^c$ as the reference, the rotation matrix $\boldsymbol{T}$ and translation vector $\boldsymbol{t}$ of the right camera coordinate system $o_r^c - x_r^c y_r^c z_r^c$ with respect to the left camera are obtained through stereo calibration.

(3) The pixel coordinate systems of the left and right cameras are denoted by $u_l v_l$ and $u_r v_r$, respectively, and the corresponding normalized image coordinate systems are $o_l^n - x_l^n y_l^n z_l^n$ and $o_r^n - x_r^n y_r^n z_r^n$.

(4) The camera-side surface and the object-side surface of the protective layer serve as refractive interfaces. Both interfaces are planar and parallel to each other. Their unit normal vector is denoted by $\boldsymbol{N}$. The thickness of the protective layer is $\boldsymbol{d}$, and the distance from the camera-side surface to the optical centre of the left camera along the direction of $\boldsymbol{N}$ is D. The parameters $\boldsymbol{N}$, d and D can be obtained through calibration (Sun et al., 2024).

(5) The protective layer is a transparent flat plate, and the refractive indices of air and the protective material are known.

2.2 Ray tracing through the planar layer

During measurement, the stereo cameras capture images of the target, and the pixel coordinates of point P are obtained. In the left and right pixel coordinate systems, the projections of point P are denoted as points L_1 and R_1, with coordinates $\boldsymbol{L}_1$ and $\boldsymbol{R}_1$, respectively, which are obtained through target detection and matching. In the normalized image planes, the corresponding points of P are denoted as L_2 and R_2, whose coordinates can be computed as

$$\begin{cases} \boldsymbol{L}_2 = \boldsymbol{K}_l^{-1}\boldsymbol{L}_1 \\ \boldsymbol{R}_2 = \boldsymbol{T}\boldsymbol{K}_r^{-1}\boldsymbol{R}_1 + \boldsymbol{t} \end{cases} \tag{1}$$

To ensure consistency in matrix dimensions, $\boldsymbol{L}_1$ and $\boldsymbol{R}_1$ in the above equation are converted into homogeneous coordinates in the pixel coordinate system.

Since the four points o_l^c, L_1, L_2 and L_3 are collinear, and the four points o_r^c, R_1, R_2 and R_3 are also collinear, the unit direction vectors of the rays $o_l^c\mathrm{L}_3$ and $o_r^c\mathrm{R}_3$, denoted as $\boldsymbol{\zeta}_1$ and $\boldsymbol{\xi}_1$, respectively, can be expressed as

$$\begin{cases} \boldsymbol{\zeta}_1 = \frac{\boldsymbol{L}_2 - \boldsymbol{o}_l^c}{|\boldsymbol{L}_2 - \boldsymbol{o}_l^c|} \\ \boldsymbol{\xi}_1 = \frac{\boldsymbol{R}_2 - \boldsymbol{o}_r^c}{|\boldsymbol{R}_2 - \boldsymbol{o}_r^c|} \end{cases} \tag{2}$$

The normal vector of the camera-side surface of the protective layer is $\boldsymbol{N}$, and the distance from this surface to the optical centre of the left camera is D. According to the intersection formula between a spatial line and a plane, the coordinates of points L_3 and R_3, denoted as $\boldsymbol{L}_3$ and $\boldsymbol{R}_3$, can be expressed as

$$\begin{cases} \boldsymbol{L}_3 = \boldsymbol{o}_l^c + \frac{D - \boldsymbol{N}\cdot\boldsymbol{o}_l^c}{\boldsymbol{N}\cdot\boldsymbol{\zeta}_1}\boldsymbol{\zeta}_1 \\ \boldsymbol{R}_3 = \boldsymbol{o}_r^c + \frac{D - \boldsymbol{N}\cdot\boldsymbol{o}_r^c}{\boldsymbol{N}\cdot\boldsymbol{\xi}_1}\boldsymbol{\xi}_1 \end{cases} \tag{3}$$

Based on the direction vectors of the rays $o_l^c\mathrm{L}_3$ and $o_r^c\mathrm{R}_3$, and the normal vector of the refractive interface, the angles θ_1 and φ_1 can be expressed as

$$\begin{cases} \theta_1 = \cos^{-1}(\boldsymbol{\zeta}_1 \cdot \boldsymbol{N}^{\mathrm{T}}) \\ \varphi_1 = \cos^{-1}(\boldsymbol{\xi}_1 \cdot \boldsymbol{N}^{\mathrm{T}}) \end{cases} \tag{4}$$

Let the refractive index of air be n_1 and that of the protective layer be n_2. According to the law of refraction, the angles θ_2 and φ_2 can be expressed as

$$\begin{cases} \theta_2 = \sin^{-1}\left(\frac{n_1 \sin\theta_1}{n_2}\right) \\ \varphi_2 = \sin^{-1}\left(\frac{n_1 \sin\varphi_1}{n_2}\right) \end{cases} \tag{5}$$

Based on the spatial vector rotation formula, the direction vectors of the rays $\mathrm{L}_3\mathrm{L}_4$ and $\mathrm{R}_3\mathrm{R}_4$, denoted as $\boldsymbol{\zeta}_2$ and $\boldsymbol{\xi}_2$, respectively, can be expressed as

$$\begin{cases} \boldsymbol{\zeta}_2 = \frac{n_1}{n_2}\boldsymbol{\zeta}_1 - \left(\frac{n_1}{n_2}\cos\theta_1 - \cos\theta_2\right)\boldsymbol{N} \\ \boldsymbol{\xi}_2 = \frac{n_1}{n_2}\boldsymbol{\xi}_1 - \left(\frac{n_1}{n_2}\cos\varphi_1 - \cos\varphi_2\right)\boldsymbol{N} \end{cases} \tag{6}$$

Similarly, according to the intersection formula between a spatial line and a plane, the coordinates of points L_4 and R_4, denoted as $\boldsymbol{L}_4$ and $\boldsymbol{R}_4$, can be expressed as

$$\begin{cases} \boldsymbol{L}_4 = \boldsymbol{L}_3 + \frac{D + d - \boldsymbol{N}\cdot\boldsymbol{L}_3}{\boldsymbol{N}\cdot\boldsymbol{\zeta}_2}\boldsymbol{\zeta}_2 \\ \boldsymbol{R}_4 = \boldsymbol{R}_3 + \frac{D + d - \boldsymbol{N}\cdot\boldsymbol{R}_3}{\boldsymbol{N}\cdot\boldsymbol{\xi}_2}\boldsymbol{\xi}_2 \end{cases} \tag{7}$$

The two surfaces of the protective layer are planar and parallel to each other. Therefore, the ray $o_l^c\mathrm{L}_3$ is parallel to $\mathrm{L}_4\mathrm{P}$, and the ray $o_r^c\mathrm{R}_3$ is parallel to $\mathrm{R}_4\mathrm{P}$. The directions of light $\mathrm{L}_4\mathrm{P}$ and $\mathrm{R}_4\mathrm{P}$

remain $\boldsymbol{\zeta}_1$ and $\boldsymbol{\xi}_1$ respectively. So, the spatial equations of the rays L_4P and R_4P can be expressed as

$$\begin{cases} F(\tau_l) = \boldsymbol{L}_4 + \tau_l \boldsymbol{\zeta}_1 \\ F(\tau_r) = \boldsymbol{R}_4 + \tau_r \boldsymbol{\xi}_1 \end{cases} \tag{8}$$

Where τ_l, τ_r = scalar parameters of the lines

2.3 3D reconstruction

Ideally, the target point P is located at the intersection of rays L_4P and R_4P. Its 3D coordinates can be theoretically derived from the intersection of two spatial lines. However, measurement noise usually results in skew lines. Consequently, the midpoint of the common perpendicular between L_4P and R_4P is adopted as the estimated position of P. Let $P_1 \in L_4P$ and $P_2 \in R_4P$; if P_1P_2 represents the common perpendicular, the vector $\boldsymbol{P}_1 - \boldsymbol{P}_2$ must be perpendicular to both $\boldsymbol{\zeta}_1$ and $\boldsymbol{\xi}_1$, such that

$$\begin{cases} (\boldsymbol{L}_4 + \tau_l \boldsymbol{\zeta}_1 - \boldsymbol{R}_4 - \tau_r \boldsymbol{\xi}_1) \cdot \boldsymbol{\zeta}_1 = 0 \\ (\boldsymbol{L}_4 + \tau_l \boldsymbol{\zeta}_1 - \boldsymbol{R}_4 - \tau_r \boldsymbol{\xi}_1) \cdot \boldsymbol{\xi}_1 = 0 \end{cases} \tag{9}$$

Solving Eq. (9) gives

$$\begin{cases} \tau_l = \frac{B \cdot C - B \cdot E}{A \cdot C - B^2} \\ \tau_r = \frac{A \cdot E - B \cdot D}{A \cdot C - B^2} \end{cases} \tag{10}$$

where the parameters are

$$\begin{cases} A = \boldsymbol{\zeta}_1 \cdot \boldsymbol{\zeta}_1 \\ B = \boldsymbol{\zeta}_1 \cdot \boldsymbol{\xi}_1 \\ C = \boldsymbol{\xi}_1 \cdot \boldsymbol{\xi}_1 \\ D = (\boldsymbol{R}_4 - \boldsymbol{L}_4) \cdot \boldsymbol{\zeta}_1 \\ E = (\boldsymbol{R}_4 - \boldsymbol{L}_4) \cdot \boldsymbol{\xi}_1 \end{cases} \tag{11}$$

By substituting the line coefficients from Eq. (10) into Eq. (8), the endpoints of the common perpendicular, $\boldsymbol{P}_1$ and $\boldsymbol{P}_2$, are obtained. The target position is defined as the mean of these two points

$$\boldsymbol{P} = \frac{\boldsymbol{P}_1 + \boldsymbol{P}_2}{2} \tag{12}$$

Thus, $\boldsymbol{P}$ is the 3D position of the target, reconstructed via binocular vision while considering the planar protective layer.

3. Simulation-based Analysis of the Refraction Effects

3.1 Simulation Setup

The refractive effect is governed by parameters such as the thickness, pose (normal vector), and distance from the camera of the planar protective layer. Through simulation experiments, the influence of these various refractive parameters on the resulting refraction effects is quantitatively analysed. In the simulation, the effective horizontal and vertical fields of view are both assumed to be 60°. Target planes are positioned at four distinct distances from the camera: 2 m, 6 m, 12 m, and 20 m. Each plane contains a 41 × 41 grid, where each grid point represents an individual target. For convenience, the distance between the target plane and the camera is hereafter denoted by S. When $S = 2$ m, the distribution of the targets in the left camera coordinate system is shown in Figure 2. The simulation ignores camera lens distortion; the intrinsic parameters for the left and right cameras are listed in Table 1, while the extrinsic parameters of the right camera relative to the left are provided in Table 2.

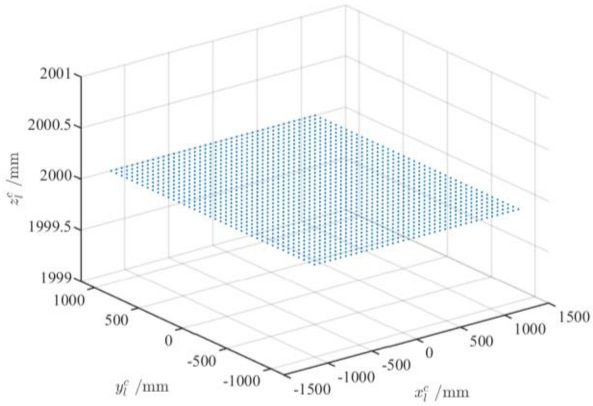

Figure 2. The distribution of the targets in the left camera coordinate system when $S = 2$ m

Camera	f_x/Pixel	f_y/Pixel	c_x/Pixel	c_y/Pixel
Left	1157.937	1158.217	781.765	781.841
Right	1157.811	1158.817	783.711	783.070

Table 1. Intrinsic parameters of the two cameras

Rotation matrix $\boldsymbol{T}$	Translation vector $\boldsymbol{t}$/mm
$\begin{bmatrix} 1 & 0 & 0 \\ 0 & 1 & 0 \\ 0 & 0 & 1 \end{bmatrix}$	$[100 \quad 0 \quad 0]$

Table 2. Extrinsic parameters of the right camera relative to the left camera

The workflow of the simulation experiment is as follows:

(1) Pixel coordinate simulation. Based on the target coordinates, camera internal and external parameters, and defined refraction parameters, the pixel coordinates of the targets for both left and right cameras are simulated within the left camera coordinate system. These pixel coordinates serve as the ground truth and are free of measurement error.

(2) Refraction-Compensated Reconstruction. The simulated pixel coordinates are processed based on the binocular vision measurement principle that accounts for the planar protective layer, yielding the reconstructed target coordinates.

(3) Conventional triangulation. Ignoring the influence of the protective layer, the pixel coordinates are processed directly via standard triangulation to obtain the target coordinates.

(4) Comparative analysis. The relationship between the target coordinates obtained from both methods—accounting for and ignoring the protective layer—and the ground truth target coordinates is calculated and analysed.

3.2 Simulation I: Analysis of the Impact of Target-to-Camera Distance

The normal vector $\boldsymbol{N}$ of the protective layer surface, the thickness d, the distance D from the left camera's optical center to the inner surface of the layer, and the target-to-camera distance S are summarized in Table 3. For $S = 2$ m, the differences between the ground truth coordinates and the results obtained by both methods—accounting for and ignoring the protective layer—are shown in Figure 3. It can be seen that when the refractive effects are taken into account, the differences between the simulated 3D coordinates and the ground truth are on the magnitude of 10^{-10}

mm. This negligible discrepancy primarily stems from numerical rounding errors, suggesting that the two are numerically identical. This validates the correctness of the established refractive imaging model and its corresponding solution method. In contrast, when the refractive effects are ignored and the ideal pinhole model is used directly, the systematic bias in the target coordinates increases significantly. Specifically, the maximum errors in the x_i^c and y_i^c coordinates are approximately ± 0.5 mm, while the error in the z_i^c coordinate along the optical axis is notably more pronounced, with a maximum value exceeding 5 mm. This indicates that the depth direction is particularly sensitive to the refraction introduced by the protective layer. Failing to apply refractive corrections will result in significant scale distortion in the 3D reconstruction results.

$\boldsymbol{N}$	d/mm	D/mm	S/m
[0 0 1]	10	100	2, 6, 12, 20

Table 3. Parameters of simulation experiment I

When the target plane is located at distances of 6 m, 12 m, and 20 m from the camera, the experimental results exhibit variation patterns similar to those shown in Figure 3. When the effect of the protective layer is taken into account, the simulated coordinates of the target agree well with the ground-truth values. In contrast, when the influence of the protective layer is neglected, significant coordinate discrepancies still exist. The magnitude of these discrepancies depends not only on the viewing position of the target point on the image plane, but also strongly on the distance between the target plane and the camera.

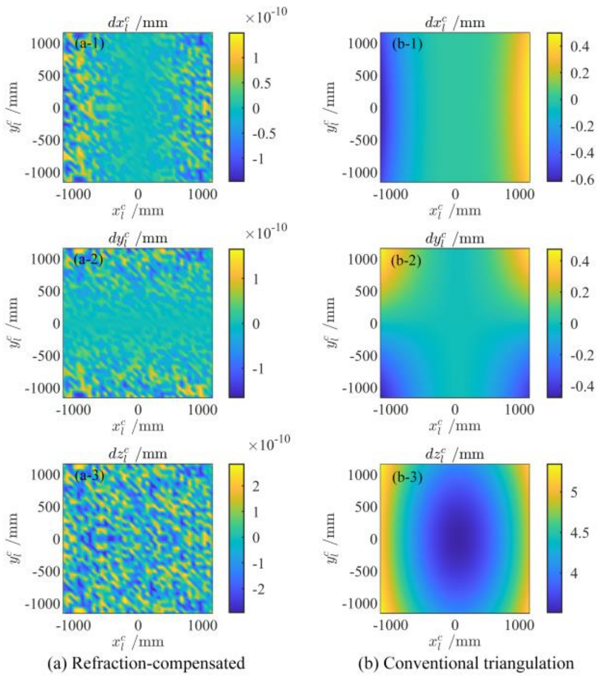

Figure 3. The coordinate differences of simulation experiment I when S=2 m

To further analyse the relationship between the coordinate error of the target and the distance S between the target and the camera when the refraction effect of the protective layer is neglected, eight representative target points listed in Table 4 are selected for comparative analysis. The selected targets include the four corner points and the midpoints of the four edges of a square field of view (FOV), which can comprehensively reflect the distribution characteristics of refraction errors in different viewing directions.

Objects	Horizontal angle/°	Vertical angle /°
P_1	-60	0
P_2	-60	-60
P_3	0	-60
P_4	60	-60
P_5	60	0
P_6	60	60
P_7	0	60
P_8	-60	60

Table 4. Perspective of specific objects

The variation of the coordinate differences of these eight target points with respect to the distance S is shown in Figure 4. It can be observed that, for non-zero coordinate components, the coordinate difference varies with the distance between the target and the camera, exhibiting a clear distance-dependent characteristic. Specifically, the closer the target is to the camera, the faster the coordinate difference changes; as the target moves farther away, the rate of change gradually decreases. Meanwhile, the directional characteristics of the coordinate difference with respect to distance are relatively complex. As the target gradually moves away from the camera, the coordinate difference may either increase or decrease, and its variation trend is closely related to the position of the target within the FOV. The variation patterns of refraction error with distance differ significantly for targets in different viewing directions, indicating that the refraction effect exhibits pronounced spatial non-uniformity across the FOV.

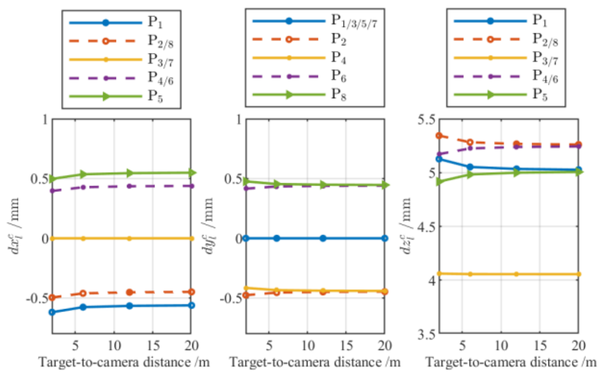

Figure 4. Coordinate difference varies with the change of the target-to-camera distance

A comprehensive analysis indicates that when a planar protective layer is present in front of the camera and the conventional ideal stereo vision model in air is still used for reconstruction, the influence of refraction on the measurement results depends not only on the distance between the target and the camera, but also strongly on the direction of the target within the FOV. Targets located in different directions are affected by refraction to varying degrees, and the impacts on the three components of the 3D coordinates also differ significantly. Among them, the depth component is the most sensitive to the refraction effect, with errors reaching the millimetre level, whereas the lateral and longitudinal components are relatively less affected. In addition, the coordinate differences induced by refraction exhibit a clear nonlinear dependence on the target distance. For targets in different directions, the variation patterns of error with distance are not consistent; even for the same target, the error trends differ among coordinate components. Nevertheless, from an overall perspective, the closer the target is to the camera, the more rapidly the influence of refraction on the measurement results changes.

https://doi.org/10.5194/isprs-archives-XLIX-B2-2026-1043-2026

In close-range, high-precision applications such as structural deformation monitoring, even when the target is located at the centre of the FOV, neglecting the refraction induced by the protective layer may introduce non-negligible systematic errors. Therefore, under imaging conditions involving a planar protective layer, the refraction effect is one of the key factors affecting the accuracy of stereo vision-based 3D measurements. If the refraction of the protective layer is ignored, non-negligible systematic errors will be introduced. In contrast, by establishing a refraction-aware imaging model that accounts for the protective layer, such systematic errors can be effectively eliminated.

3.3 Simulation II: Analysis of the Impact of Protective Layer-to-Camera Distance

The normal vector $\boldsymbol{N}$ of the protective layer surface, the thickness d of the protective layer, the distance D from the optical centre of the left camera to the camera-side surface of the protective layer, and the distance between the target and the camera are listed in Table 5. The distance D from the camera-side surface of the protective layer to the optical centre is set to three different values.

The experimental results show that, for different values of D, the resulting distributions of target coordinate differences are consistent with those shown in Figure 3. This indicates that the stereo vision measurement algorithm that accounts for the planar protective layer can effectively eliminate the influence of refraction, whereas the conventional stereo vision model in air is affected by refraction to a fixed extent that is independent of D. In other words, variations in the distance between the camera optical centre and the inner surface of the protective layer do not alter the fundamental characteristics of the refraction-induced error. This is because the imaging deviation caused by refraction is primarily determined by the normal direction of the refractive interface and the difference in refractive indices between media. The distance between the camera optical centre and the inner surface of the protective layer only changes the location where refraction occurs, but does not affect the relationship between the incident angle and the refracted angle. Therefore, the systematic error introduced by the refraction effect is insensitive to D.

3.4 Simulation III: Analysis of the Impact of Protective Layer Attitude

The normal vector $\boldsymbol{N}$ of the protective layer surface, the thickness d of the protective layer, the distance D from the optical centre of the left camera to the camera-side surface of the protective layer, and the distance S between the target and the camera are listed in Table 6. Three configurations of $\boldsymbol{N}$ are considered: when the refractive interface is perpendicular to the z_l^c-axis of the left camera coordinate system, the normal vector is denoted as $\boldsymbol{N}_1$; when the interface is rotated by 5° about the x_l^c-axis, the normal vector is $\boldsymbol{N}_2$; and when it is rotated by 5° about the y_l^c-axis, the normal vector is $\boldsymbol{N}_3$.

The experimental results obtained by neglecting the refraction effect of the protective layer are shown in Figure 5. It can be observed that changes in the orientation of the planar protective layer lead to significant variations in the systematic errors of the stereo measurement system. First, when the refractive interface deviates from the perpendicular configuration, the differences between the measured values and the ground-truth values exhibit pronounced systematic biases. These biases arise from the nonlinear distortion induced by the tilted refractive interface, which alters the distribution of incidence angles as light propagates across media. Consequently, the projection positions of object points on the image plane experience asymmetric shifts, ultimately resulting in systematic distortions in the reconstructed 3D coordinates. Second, regardless of the orientation of the refractive interface, the measurement error decreases as the radial distance of the target point from the centre of the FOV decreases. In other words, near the centre of the FOV, the rays approach normal incidence, and the refraction-induced deviation is minimal. As the target moves toward the edge of the FOV, the increasing incidence angle leads to a nonlinear amplification of the refraction effect.

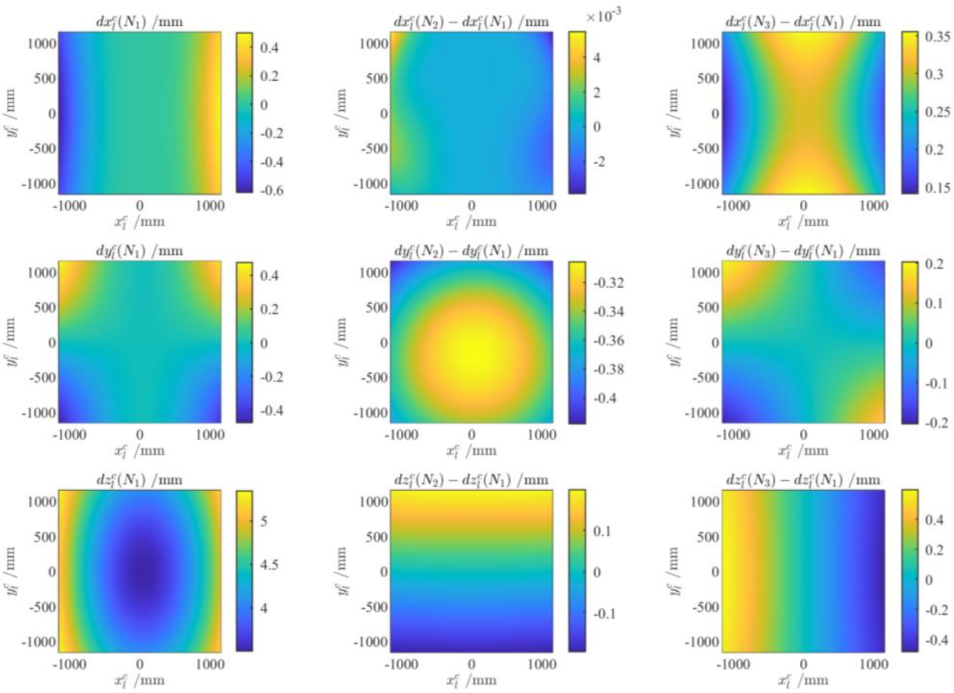

Figure 5. Results of simulation experiment III

$\boldsymbol{N}$	d/mm	D/mm	S/m
$[0 \quad 0 \quad 1]$	10	100, 500, 1000	2

Table 5. Parameters of Simulation II

$\boldsymbol{N}$	d/mm	D/mm	S/m
$\boldsymbol{N}_1 = [0 \quad 0 \quad 1]$ $\boldsymbol{N}_2 = [0 \quad -0.0872 \quad 0.9962]$ $\boldsymbol{N}_3 = [0.0872 \quad 0 \quad 0.9962]$	10	100	2

Table 6. Parameters of Simulation III

3.5 Simulation IV: Analysis of the Impact of Protective Layer Thickness

The normal vector $\boldsymbol{N}$ of the protective layer surface, the thickness d of the protective layer, the distance D from the optical centre of the left camera to the camera-side surface of the protective layer, and the distance S between the target and the camera are listed in Table 7. Four different thicknesses of the protective layer are considered.

$\boldsymbol{N}$	d/mm	D/mm	S/m
$[0 \quad 0 \quad 1]$	10, 5, 2.5, 1	100	2

Table 7. Parameters of Simulation IV

The experimental results are shown in Figure 6. It can be observed that, when the refraction effect of the protective layer is neglected, the coordinate differences of the target exhibit a significant positive correlation with the thickness of the protective layer. For all coordinate components, the coordinate differences decrease approximately linearly as the thickness d decreases. From the perspective of geometrical optics, the thickness d directly determines the lateral displacement of light as it propagates through the protective layer. The thinner the layer, the smaller the deviation between the emergent ray path after refraction and the ideal path (without the protective layer), thereby reducing the point displacement induced by the refraction effect.

Regardless of variations in the thickness of the protective layer, the spatial distribution of coordinate discrepancies remains highly consistent across the FOV. Specifically, the coordinate difference exhibits a non-linear increasing trend from the centre toward the periphery of the FOV, with the smallest errors occurring near the centre. Quantitative analysis reveals that even with a layer thickness of only 1 mm, the depth coordinate error induced at the centre of the FOV still reaches approximately 0.4 mm.

4. Field Experiment

To verify the effectiveness and robustness of the proposed binocular vision measurement model under real-world conditions, 3-D reconstruction comparison field experiments were designed and conducted. Regarding hardware selection, an Intel RealSense D455 stereo camera was employed as the imaging terminal, with the image resolution set to 1280×800 pixels. The protective layer consisted of a 10 mm thick parallel-plane PMMA (acrylic) plate, representing a typical thickness for protective windows in harsh environments. A precision 11×8 checkerboard was used as the target plane, providing 88 checkerboard corner points as the target points for measurement. The experiments were carried out in two distinct kinds of environment: outdoor and basement parking. The experimental system configuration is illustrated in Figure 7(a), and the various observation conditions are summarized in Table 8.

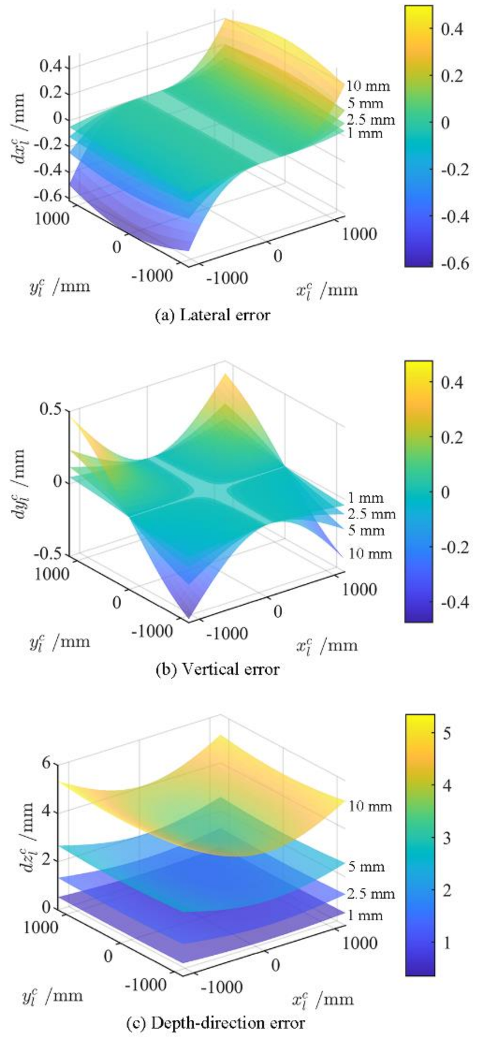

Figure 6. Variation of coordinate errors with protective-layer thickness

Experiment No.	Scene	S/m	Protective Layer Attitude
I	Outdoor	1.5	Perpendicular to the optical axis of the left camera
II	Basement parking	2	Perpendicular to the optical axis of the left camera
III	Basement parking	3	Perpendicular to the optical axis of the left camera
IV	Basement parking	2	Rotate 10° clockwise around the y_l^c axis of the left camera

Table 8. The various observation conditions of field experiments

The experiment utilized the left camera coordinate system as the reference frame, with both the camera's intrinsic parameters and the binocular baseline length pre-determined through precision calibration. The refractive index of the PMMA plate was set to 1.49 (Wildner and Drummer, 2018). The normal vector of the refractive interface and its offset distance from the camera's optical centre are the core structural parameters of the refraction correction model. To achieve high-precision external calibration of these parameters, an auxiliary checkerboard target of negligible thickness was attached to the camera-side surface of the PMMA plate at the beginning of the experiment, as shown in Figure 7(b). Since the target was flush with the medium surface, its plane is geometrically equivalent to the refractive interface. Using conventional binocular vision measurement algorithms in an air environment, the 3-D coordinates of each checkerboard corner point on the target were extracted and reconstructed. Subsequently, a plane-fitting procedure was performed on the reconstructed point cloud based on the least-squares criterion to solve for the optimal fitting equation of the target plane. The directional coefficients of the equation constitute the normal vector of the protective layer surface, while the intercept term corresponds to the vertical distance from the camera’s optical centre to the refractive interface. The advantage of this geometric calibration scheme for the PMMA plate lies in the direct alignment of the refractive interface parameters with the camera coordinate system.

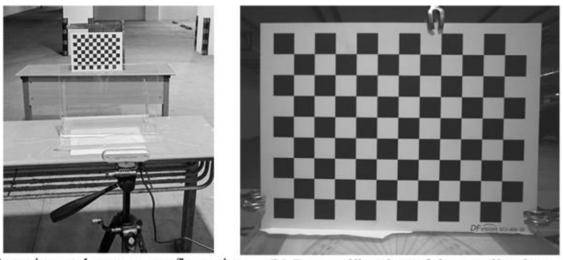

(a) Experimental system configuration (b) Pose calibration of the acrylic plate

Figure 7. Experimental system configuration and imaging

To objectively evaluate the performance of the proposed binocular vision measurement model that accounts for a planar protective layer, the experimental procedure is designed as follows. First, an acrylic protective layer is installed in front of the camera to simulate a real cross-media observation scenario. The left and right cameras synchronously acquire images of the target points. Two reconstruction strategies are then applied to process the captured images. The first strategy employs a conventional air-based binocular vision measurement algorithm to reconstruct the 3D coordinates of the target points; the results are used as a control group to assess the magnitude of positional deviations caused by refraction effects. The second strategy adopts the proposed binocular vision measurement model that accounts for the planar protective layer, serving as the experimental group. Then, while keeping the camera poses and target positions strictly unchanged, the acrylic protective layer is removed, allowing the cameras to directly image the target. The 3D coordinates of the feature points computed using the conventional air-based binocular vision algorithm are defined as the reference ground truth for the experiment.

The field experimental results are shown in Figure 8. It can be observed that if the refraction effect caused by the planar protective layer is ignored, the binocular reconstruction results in different scenarios exhibit certain systematic deviations. For the horizontal and vertical coordinate components, the mean deviations of all target points are within ±0.5 mm, whereas the mean deviation of the depth coordinate component exceeds 3 mm, verifying that the depth direction is most significantly affected by refraction. These results indicate that under cross-media measurement conditions, the refraction effect introduced by the protective layer cannot be neglected. After accounting for the refraction effect of the protective layer, the reconstruction deviations are randomly distributed around the 0 mm reference line, and the systematic bias is effectively suppressed. The mean deviations in all three directions converge to within ±0.1 mm, and the fluctuation ranges of the three coordinate difference components are significantly reduced. The experimental results clearly demonstrate that by establishing a rigorous refractive measurement model, the refraction effect introduced by the parallel protective layer can be accurately compensated, thereby improving the accuracy of cross-media 3D reconstruction.

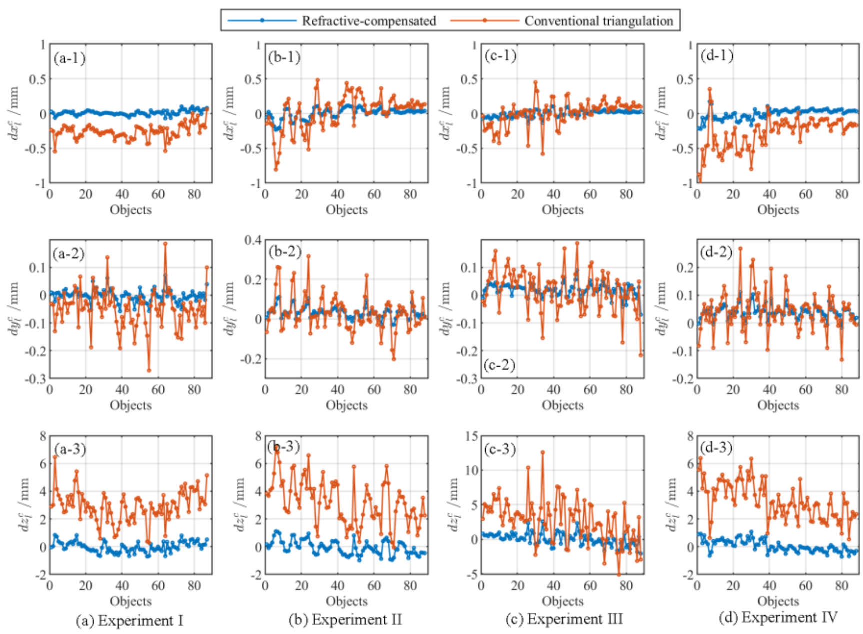

Figure 8. Coordinate differences of field experiments

https://doi.org/10.5194/isprs-archives-XLIX-B2-2026-1043-2026 |

By comparing the field experimental results with those presented in Section 3, it can be observed that both kinds of experiments exhibit a high degree of consistency and complementarity in terms of the distribution characteristics of coordinate differences, the effectiveness of model correction, and parameter sensitivity. Both the simulation and field experiments confirm that neglecting the refraction effect introduced by the planar protective layer leads to significant systematic deviations in the 3D reconstruction results, with the depth direction being the most sensitive to refraction. The two types of experiments provide mutual validation of the effectiveness of the binocular refractive vision measurement model. Under simulated conditions, the computed results considering refraction are numerically identical to the ground truth. Under real measurement conditions, however, the reconstruction accuracy is further affected by several factors, including camera parameter calibration errors, measurement errors of the protective layer’s geometric parameters (such as the surface normal and thickness of the protective layer), and subpixel extraction errors of objects. As a result, the obtained coordinate deviations are randomly distributed around the 0 mm reference line, with the residual errors significantly reduced.

The simulation experiments provide rigorous theoretical verification and full-field sensitivity analysis for the refractive imaging model, while the real-world experiments validate the practical applicability of the model under different types of physical environments. In practical operations where a planar protective layer is present, the accuracy of the binocular vision measurement model that accounts for the protective layer can be further improved by performing more rigorous calibration of the camera and protective layer geometric parameters, as well as optimizing target detection and matching algorithms to reduce observation noise (Wu et al., 2025).

5. Conclusions

This study investigates the air–protective layer–air medium configuration commonly encountered in engineering applications. The refractive effects introduced by a planar protective layer in binocular vision measurement are analysed, and the effectiveness of a refraction correction model is validated through simulation and field experiments. Results indicate that the presence of a planar protective layer introduces significant systematic refractive deviations when conventional air-based binocular models are used. Errors may reach the millimetre level, with the depth component being the most sensitive. The deviation varies nonlinearly with viewing angle and target distance, with smaller errors near the centre of the field of view and larger errors near the edges. The magnitude and spatial distribution of the refractive deviations are strongly influenced by the protective layer parameters, including target distance, layer pose, and thickness, whereas the distance between the protective layer and the camera has negligible influence. The proposed refraction correction model effectively compensates for these errors. In simulations, corrected deviations are close to zero, while field experiments show significant reductions in systematic errors across all coordinate directions, with reconstructed results closely matching the ground truth. Accurate calibration of refractive parameters, such as the surface normal and thickness of the protective layer, is essential for reliable binocular vision measurements in complex environments.

References

Chen, I., Ho, S. and Su, M., 2020. Computer vision application programming for settlement monitoring in a drainage tunnel. *Automation in Construction*, 110.

Hu, Q., Wang, K., Ren, F. and Wang, Z., 2024. Research on underwater robot ranging technology based on semantic segmentation and binocular vision. *Scientific reports*, 14(1): 12309.

Li, G., Huang, S., Yin, Z., Zheng, N. and Zhang, K., 2024. Analysis of the Influence of Refraction-Parameter Deviation on Underwater Stereo-Vision Measurement with Flat Refraction Interface. *Remote Sensing*, 16(17): 3286.

Li, S., Xie, X. and Zhuang, Y., 2018. Research on the calibration technology of an underwater camera based on equivalent focal length. *Measurement*, 122: 275-283.

Su, Z., Pan, J., Lu, L., Dai, M., He, X. and Zhang, D., 2021. Refractive three-dimensional reconstruction for underwater stereo digital image correlation. *Optics Express*, 29(8): 12131.

Sun, Y., Zhou, T., Zhang, L. and Chai, P., 2024. Underwater Camera Calibration Based on Double Refraction. *Journal of Marine Science and Engineering*, 12(5): 842.

Tong, Z., Gu, L. and Shao, X., 2023. Refraction error analysis in stereo vision for system parameters optimization. *Measurement*, 222: 113650.

Treibitz, T., Schechner, Y., Kunz, C. and Singh, H., 2012. Flat Refractive Geometry. *IEEE Transactions on Pattern and Machine Intelligence*, 34(1): 51-65.

Wildner, W. and Drummer, D., 2018. Analysis of the processing-pressure dependent refractive index of Poly(methyl methacrylate) by transmission measurements of glass-filled specimen. *Polymer Testing*, 71: 217-222.

Wu, T., Hou, S., Sun, W., Shi, J., Yang, F., Zhang, J., Wu, G. and He, X., 2023. Visual measurement method for three-dimensional shape of underwater bridge piers considering multirefraction correction. *Automation in Construction*, 146: 104706.

Wu, T., Hou, S., Wu, Z., Xiong, W., Zhang, J., Shao, X., He, X. and Wu, G., 2025. Underwater bridge pier morphology measurement method via refraction correction and multi-camera calibration. *Computer-Aided Civil and Infrastructure Engineering*, 40(16): 2324-2350.

Yang, W., Zhang, X., Ma, H. and Zhang, G., 2021a. Geometrically Driven Underground Camera Modeling and Calibration With Coplanarity Constraints for a Boom-Type Roadheader. *IEEE Transactions on Industrial Electronics*, 68(9): 8919-8929.

Yang, W., Zhang, X., Ma, H., Zhang, G. and Yang, G., 2021b. Non-central refractive camera calibration using co-planarity constraints for a photogrammetric system with an optical sphere cover. *Optics and Lasers in Engineering*, 139.

Zhan, Y., Huang, Y., Fan, Z., Li, B., An, J., Shao, J. and Tian, Y., 2024. Computer Vision-Based Pier Settlement Displacement Measurement of a Multispan Continuous Concrete Highway Bridge under Complex Construction Environments. *Structural Control & Health Monitoring*, 2024.